Regular Article

Selected issues of phase-field crystal simulations

H. Emmerich[1,a], L. Gránásy[2,3], and H. Löwen[4]

[1] Materials and Process Simulation, University of Bayreuth, Germany
[2] Research Institute for Solid State Physics and Optics - P.O. Box 49, H-1525 Budapest, Hungary
[3] BCAST, Brunel University - Uxbridge, Middlesex UB 8 3PH, UK
[4] Institut für Theoretische Physik II: Weiche Materie, Heinrich-Heine-Universität Düsseldorf - D-40225 Düsseldorf, Germany

Abstract. In this contribution our focus is on the phase-field crystal method, which can be viewed as the youngest methodology in the field of interface computation based on recent work by Elder *et al.* (Phys. Rev. Lett. **88**, 245701 (2002)). It bridges the gap between the molecular simulation approaches and the phase-field approach by operating on diffusive time scales yet atomic length scales. Here we review the fundaments of the phase-field crystal method as well as different models established so far with the aim to capture the main features of the wide range of phase diagrams found in materials science more and more comprehensively.

1 Introduction to the phase-field crystal method

In the context of this volume on interface computation across the scales the phase-field crystal method is certainly the most recent methodological development to be reported. Interestingly, at the same time it deserves a special slot in the volume, since it bridges the gap between the molecular simulation approaches and the phase-field approach by operating on diffusive time scales yet atomic length scales. Since it inherits the variational principles for model equations' derivation from the phase-field method, let us introduce it via comparison to the phase-field method, which by now has become an accepted model approach for studying the interfacial dynamics of systems out of equilibrium [1]. In particular, it has found numerous applications for the evolution of interfaces in materials science [1–4]. A classical example of such an application is solidification: Consider a material that is disordered at high temperature and has two stable phases at low temperatures. Upon quenching the material from a high to a low temperature, grains of different stable phases will develop and evolve in competition with each other. Phase-field modeling is able to describe the time evolution of such a process. To do so, a continuous function of space and time $\phi(\mathbf{x}, t)$ is introduced —namely the phase-field— that assumes a different constant value for both stable phases. Close to an interface between two grains, the value of ϕ changes rapidly. The phase-field variable introduced in the context of this example can be interpreted as a scalar order parameter to represent the relative mass fraction of both phases. It allows to model and simulate the dynamics of interfaces between two different phases, that change their topology during evolution in time —so-called Stefan problems [5]— elegantly, *i.e.* without the need to track that interface explicitly. To that end phase-field models are based on the following Landau form of an equilibrium free energy functional for a two-phase system:

$$F[\phi] = \int_V \left[\frac{\xi^2}{2} |\boldsymbol{\nabla}\phi|^2 + f(\phi) \right] \mathrm{d}V, \tag{1}$$

where ξ is just a scalar parameter and $f(\phi)$ the free energy density of the system in terms of ϕ. This function $f(\phi)$ can be expanded into a Taylor series, such that up to fourth order in ϕ it yields a double-well potential. Terms of uneven exponent vanish, since $f(\phi)$ is by assumption symmetric, *i.e.* the two different phases are energetically equal. As a consequence $f(\phi)$ is invariant to the transformation $\phi \to -\phi$. If the two minima of $f(\phi)$ define the energy level 0 and occur at ± 1, then $f(\phi)$ reads

$$f(\phi) = \frac{f_0}{4}(\phi^2 - 1)^2 \,, \tag{2}$$

with a scale factor f_0.

---

[a] e-mail: heike.emmerich@uni-bayreuth.de

To be able to consider *inhomogeneous* states as well, the energy density functional has to depend also on the gradient of the phase-field variable. Lowest-order terms which are compatible with invariance under rotation and translation are $\nabla^2\phi$ and $(\nabla\phi)^2$. For the calculation of $F[\phi]$ the relevant volume integrals of the two terms are identical apart from a surface integral. This surface integral, however, describes only boundary effects. It vanishes if the phase boundary is completely inside of the integration volume and thus can be neglected. Therefore it is sufficient to supplement $f(\phi)$ by $(\nabla\phi)^2$, yielding (1) for the full equilibrium free energy functional of the system.

It is possible to give a microscopic derivation for this functional as well. It can be obtained on the basis of a lattice model for a two-state equilibrium thermodynamic system [6–9][1]. Within such a model each of the lattice squares $\mathbf{x}$ of a rectangular grid is occupied by a variable $\phi(\mathbf{x}) \in \{-1; 1\}$. The variable ϕ distinguishes between the two possible states. For the energy of a given configuration the following ansatz is chosen:

$$E = -\frac{1}{2}\sum_{\mathbf{x},\mathbf{x}'} J(\mathbf{x}-\mathbf{x}')\phi(\mathbf{x})\phi(\mathbf{x}') - H\sum_{\mathbf{x}}\phi(\mathbf{x})\,. \tag{3}$$

The first term denotes the interaction energy originating from the coupling term $J(\mathbf{x}-\mathbf{x}')$, the second term contains the energy contribution from external fields.

If ϕ is treated as a continuous variable, it is necessary to include an additional function $W(\phi(\mathbf{x}))$ due to entropy. W is a weight function which determines the physically favored values of ϕ. With the introduction of W one obtains the Landau-Ginzburg-Wilson functional as

$$F = -\frac{1}{2}\sum_{\mathbf{x},\mathbf{x}'} J(\mathbf{x}-\mathbf{x}')\phi(\mathbf{x})\phi(\mathbf{x}') - H\sum_{\mathbf{x}}\phi(\mathbf{x}) + \sum_{\mathbf{x}} W(\phi(\mathbf{x}))\,. \tag{4}$$

For $W(\phi(\mathbf{x}))$ a symmetric potential with second- and fourth-order terms is the suitable form to describe a two-state system. For the case of a short-range interaction $J(\mathbf{x}-\mathbf{x}')$ (*e.g.*, nearest neighbor interaction) as well as vanishing external fields, (4) can be transformed into an equation analogous to (1) [6,9]. Thus for *thermodynamic equilibrium* microscopic and macroscopic derivation yield the same ansatz for F. Furthermore the microscopic approach provides additional insight into the nature of diffuse interface models. It yields an understanding, that the finite interface thickness of a diffuse interface model and the surface energy term originate from finite correlation lengths on a microscopic scale. Moreover —assuming nearest neighbor interaction and constant coupling constant J— interface thickness and surface energy are proportional to J.

For non-equilibrium conditions a coherent microscopic derivation is missing. From a macroscopic point of view, (1) can be extended to account for non-equilibrium conditions by introducing a further energetic term $M(\phi)$ such that

$$F(\phi) = \frac{\xi^2}{2}(\nabla\phi)^2 + f(\phi) + M(\phi)\,. \tag{5}$$

The contribution $M(\phi)$ depends on the special physical properties of the system under consideration, *e.g.*, the underlying phase diagram. Together with $f(\phi)$ this additional term M results in a double-well potential, which is no longer symmetrical with respect to $\phi \to -\phi$. The dynamic equations obtained from (5) owe the driving force, which moves the interface, to the term $M(\phi)$. In this context the evolutionary equation for the phase-field variable ϕ can be interpreted as a mean-field approximation of the non-equilibrium interface dynamic. Formally this evolution equation can be obtained based on the principles of irreversible thermodynamics (see [1], sect. 4.1, for details) via a variation of the form

$$\frac{\partial\phi}{\partial t} = \nabla^2\frac{\delta F_i}{\delta\phi}\,, \tag{6}$$

or

$$\frac{\partial\phi}{\partial t} = -\frac{\delta F_i}{\delta\phi}\,, \tag{7}$$

depending on whether ϕ can be assumed to be *locally conserved* (eq. (6)) or *locally non-conserved* (eq. (7)), respectively,

$$\frac{\partial\phi}{\partial t} = \nabla^2\frac{\delta F_i}{\delta\phi} + \eta \tag{8}$$

or

$$\frac{\partial\phi}{\partial t} = -\frac{\delta F_i}{\delta\phi} + \eta\,, \tag{9}$$

if we assume dissipative dynamics. Here η denotes an additional noise term in accordance to the usual Langevin formulation.

---

[1] Similar ideas allowing to formulate an atomistic counterpart for the phase-field order parameter can be found in [10–13].

A functional of form (1) applies, if the stable states of the system under investigation are uniform. If this assumption is not valid, an appropriate energy functional is given by

$$F = \int_V \left(\frac{1}{2}\phi \left[(q_0^2 + \nabla^2)^2 + a \right] \phi + \frac{1}{4}\phi^4 \right) dV, \tag{10}$$

with now two phenomenological parameters q_0 and a in dependence of which the system will assume different spatially varying bulk states. Again an equation of motion can be derived based on the variational principle (6) (respectively, (8)), which minimizes the free energy giving rise to the following dynamical equation:

$$\frac{\partial \phi}{\partial t} = -\frac{\delta F}{\delta \phi} + \eta = -(a + (q_0^2 + \nabla^2)^2)\phi - \phi^3 + \eta. \tag{11}$$

If applied, *e.g.*, to Rayleigh-Bénard convection the field ϕ denotes a linear combination of the fluid velocity perpendicular to the plates and the deviation from the linear temperature gradient between the plates. In this case the model derivation is motivated by the Swift-Hohenberg amplitude equation approach [14] formulated to describe systems, where the stable states are periodic, as, *e.g.*, the case for Rayleigh-Bénard convection. Also crystaline solid materials are periodic. This motivated Elder *et al.* [15] to apply (11) indeed to the investigation of phenomena in crystaline materials, however with a conservative equation of motion, thereby constituting the simplistic formulation of the so-called phase-field crystal method. Since its introduction, the phase-field crystal (PFC) method [15–19] has emerged as a computationally efficient alternative to molecular dynamics (MD) simulations for problems where the atomic and the continuum scale are tightly coupled. The reason is that it operates for atomic length scales and diffusive time scales. Thus for a simple application such as diffusion in gold or copper it runs 10^6–10^8 times faster than the corresponding MD calculation [20]. In that sense it provides, from point of view of multiscale materials modeling, an interesting link between the phase-field method and MD. Moreover, a connection between classical density functional theory of freezing and phase-field crystal modeling could be identified in [21,17]. Thereby a second theoretical foundation besides the Swift-Hohenberg amplitude equation approach could be established. Essentially it motivates the application of PFC models also for spatially non-uniform *non-periodic* states.

In the following sections, we briefly discuss these two concepts underlying the phase-field crystal method, *i.e.* the amplitude approach for periodic systems as well as the calibration and parametrization of the phase-field crystal method via classical density functional theory, respectively, in more detail. We then review basic steps in the further development of the model concept starting from [15], as well as their implication for phase diagram, nucleation and pattern formation computations in sects. 4 and 5. Finally we conclude with an outlook.

2 Motivation and interpretation of the phase-field crystal approach

Let us assume that we want to apply an equation of kind (11) to model phase transitions in material systems such as grain growth or epitaxial growth. What would be the main characteristics of such crystal growth processes the approach should be able to capture? In a first approach we could restrict our focus to essential features such as multiple crystal orientations, free surface and plastic deformation. Now all models that contain periodic solutions automatically contain elastic energy in the sense that it costs energy to change their wavelength. Further, multiple orientations are naturally included by insisting that the free energy functional is rotationally invariant, and dislocations naturally arise when two crystals of different orientation collide or when it is energetically favorable for them to nucleate. Moreover, we would expect the phase-diagram of stable states spanned by the two phenomenological parameters q_0 and a to mimic real thermodynamic phase-diagrams of crystaline materials.

The latter can be identified more easily if we turn from the simplistic functional above to a specific conserved version of the Swift-Hohenberg equation, namely the Brazovskii/Swift-Hohenberg equation [22], which can be written

$$F = \int \left(\frac{\phi}{2}[a + \lambda(q_0^2 + \nabla^2)^2]\phi + u\frac{\phi^4}{4} \right) dV. \tag{12}$$

Since here ϕ is assumed to be locally conserved, the dynamical equation governing the system has to be derived based on (8) resulting in

$$\frac{\partial \phi}{\partial t} = \nabla^2 \frac{\delta \mathcal{F}}{\delta \phi} + \eta = \nabla^2[(a + \lambda(q_0^2 + \nabla^2)^2)\phi + u\phi^3] + \eta. \tag{13}$$

In the context of material systems ϕ can be interpreted as a field variable related to the number density of the atoms in the system. a can be related to the driving force of the system, *i.e.* for example the undercooling. The remaining parameters —assuming η to be zero— can be derived and justified from dynamical density functional theory (see the following section 3).
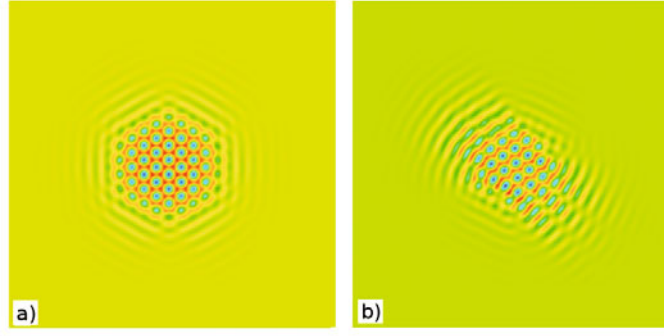
Fig. 1. Simulation results of crystal growth calculated for $\tau = -3/4$ and (a) $s = -\frac{b_{1112}}{b_{1111}} = 0$ (isotropic case) and (b) $s = 0.125$ (anisotropic case). All other parameters are chosen as given in [24].

3 Calibration of phase-field crystal models

If the above amplitude approach for periodic systems were the only theoretical fundament for the PFC approach, it could indeed only be applied to periodic systems. Materials as, *e.g.*, ellipsoidal colloids, liquid crystals and glasses with aperiodic states could not be modeled based on the PFC approach. This limitation could be overcome when a connection between classical density functional theory of freezing and phase-field crystal modeling could be identified [17,21], establishing a second theoretical fundament of the PFC approach. More precisely one may say, that the classical density functional theory allows to parametrize a given phase-field crystal model. To explain this in more detail for an extension of (12), which can give rise to anisotropic states as well based on a functional of form

$$F = \int_V \left(\frac{1}{2}\phi \left[-\tau + a_{ij}\frac{\partial^2}{\partial x_i \partial x_j} + b_{ijkl}\frac{\partial^4}{\partial x_i \partial x_j \partial x_k \partial x_l} \right] \phi + \frac{1}{4}c\phi^4 \right) \mathrm{d}r, \qquad (14)$$

where a_{ij} is a symmetric matrix and b_{ijkl} is a tensor of rank 4 with the symmetry of an elastic tensor: $i \leftrightarrow j, k \leftrightarrow l, (i,j) \leftrightarrow (k,l)$ as basis of the PFC model under consideration. Its dynamics is then given by the following partial differential equation:

$$\varrho\dot{\phi} = \Delta \left(\left[-\tau + a_{ij}\frac{\partial^2}{\partial x_i \partial x_j} + b_{ijkl}\frac{\partial^4}{\partial x_i \partial x_j \partial x_k \partial x_l} \right] \phi + c\phi^3 \right). \qquad (15)$$

This model has first been published by Prieler *et al.* in [23]. As stated above it can give rise to anisotropic morphologies as, *e.g.*, ellipsoidal colloids [23,24] (see fig. 1).

The coefficients occuring in the above anisotropic phase-field crystal can be derived from microscopic density functional theory [25–28] following a similar line as proposed recently by van Teeffelen *et al.* [21] for radially symmetric interactions. The generalization of this route to anisotropic interactions has originally been presented in [24]. It is summarized here to elucidate the basic principles underlying the parametrization of a given phase-field crystal model via density functional theory:

Let's assume that the anisotropic colloids are completely aligned in space. Cartesian coordinates $\mathbf{r} = (x_1, x_2, \ldots, x_d)$ will be used in the following, d denoting the spatial dimension. The interaction pair potential between two aligned particles is $u(\mathbf{r})$ [29]. The latter function is anisotropic, in general, *i.e.* it does not only depend on $|\mathbf{r}|$. Other examples for these anisotropic interactions with fixed orientations are oriented hard spherocylinders [30] and charged rods [31–33], anisotropic Gaussian potentials [34], board-like colloidal particles [35], colloidal molecules [36], as well as patchy colloids [37] and proteins [38,39]. Henceforth *inversion* symmetry is assumed

$$u(-\mathbf{r}) = u(\mathbf{r}). \qquad (16)$$

Dynamical density functional theory for anisotropic situations [40] is now generalized from the isotropic case as follows. The dynamical evolution of the time-dependent one-particle density field $\rho(\mathbf{r}, t)$ is:

$$\dot{\rho}(\mathbf{r}, t) = (k_B T)^{-1} \nabla \cdot \left[\overleftrightarrow{D} \rho(\mathbf{r}, t) \nabla \frac{\delta F[\rho(\mathbf{r}, t)]}{\delta \rho(\mathbf{r}, t)} \right]. \qquad (17)$$

Here $k_B T$ is the thermal energy, and $\nabla = (\partial/\partial x_1, \partial/\partial x_2, \ldots, \partial/\partial x_d)$ is the d-dimensional gradient. $\overleftrightarrow{D} = diag(D_1, D_2, \ldots, D_d)$ denotes the diagonalized diffusion tensor with the anisotropic short-time translational diffusivities of the anisotropic particle. For a given (hydrodynamic) shape of the particle, explicit expressions for D_i are available [41,42]. Furthermore, in eq. (17), $F[\rho(\mathbf{r}, t)]$ is the equilibrium density functional which can be split as

$$F[\rho(\mathbf{r})] = F_{\mathrm{id}}[\rho(\mathbf{r})] + F_{\mathrm{ex}}[\rho(\mathbf{r})] + F_{\mathrm{ext}}[\rho(\mathbf{r})], \qquad (18)$$

where

$$F_{\mathrm{id}}\left[\rho(\mathbf{r})\right] = k_B T \int \mathrm{d}\mathbf{r}\rho(\mathbf{r}) \left\{ \ln\left[\rho(\mathbf{r})\Lambda^d\right] - 1 \right\}, \tag{19}$$

with Λ denoting the thermal de Broglie wavelength. The external part involves an external one-body potential $V(\mathbf{r}, t)$ and is given by

$$F_{\mathrm{ext}}\left[\rho(\mathbf{r})\right] = \int \mathrm{d}\mathbf{r}\rho(\mathbf{r})V(\mathbf{r}, t). \tag{20}$$

Finally, the excess part $F_{\mathrm{ex}}[\rho(\mathbf{r})]$ embodies the nontrivial correlations between the particles and must be further approximated. Henceforth we assume small deviations of the inhomogeneous density profile around a homogeneous reference density ρ. In this limit, the leading approximation for $F_{\mathrm{ex}}[\rho(\mathbf{r})]$ is given by the Ramakrishnan and Yussouff [43] expression:

$$F_{\mathrm{ex}}\left[\rho(\mathbf{r})\right] \simeq F_{\mathrm{ex}}(\rho) - \frac{k_B T}{2} \iint \mathrm{d}\mathbf{r}\mathrm{d}\mathbf{r}' \Delta\rho(\mathbf{r})\Delta\rho(\mathbf{r}')c_0^{(2)}(\mathbf{r}-\mathbf{r}';\rho), \tag{21}$$

where $c_0^{(2)}(\mathbf{r}-\mathbf{r}';\rho)$ is the anisotropic direct correlation function of the fluid at density ρ which possesses the same symmetry as the underlying pair potential $u(\mathbf{r})$. In particular, it is inversion-symmetric

$$c_0^{(2)}(-\mathbf{r}, \rho) = -c_0^{(2)}(\mathbf{r}, \rho). \tag{22}$$

Moreover, $\Delta\rho(\mathbf{r}) = \rho(\mathbf{r}) - \rho$. In Fourier space eq. (21) reads

$$\mathcal{F}_{\mathrm{ex}}[\rho(\mathbf{r})] = F_{\mathrm{ex}}(\rho) - \frac{k_B T(2\pi)^d}{2} \int \mathrm{d}\mathbf{k}\Delta\tilde{\rho}(\mathbf{k})\Delta\tilde{\rho}(-\mathbf{k})\tilde{c}_0^{(2)}(\mathbf{k}, \rho) \tag{23}$$

with $\sim$ denoting a Fourier transform. We now expand the direct correlation function $c_0^{(2)}(\mathbf{k}, \rho)$ in terms of $\mathbf{k}$ around $\mathbf{k} = 0$. (Alternatively fitting procedures can be used, *e.g.*, around the first peak of $c_0^{(2)}(\mathbf{k}, \rho)$.) This leads to the Taylor expansion in Fourier space

$$\tilde{c}_0^{(2)}(\mathbf{k}, \rho) = \hat{C}_0 + \sum_{i,j=1}^{d} a_{ij}k_i k_j + \sum_{i,j,k,l=1}^{d} b_{ijkl}k_i k_j k_k k_l + \ldots \tag{24}$$

corresponding to a gradient expansion in real space. Inversion symmetry (22) enforces all odd orders to vanish. Possible additional symmetries in the shape of the particles will lead to corresponding restrictions on the tensorial coefficients a_{ij} and b_{ijkl} as discussed below.

Inserting this expansion into eq. (17), one gets

$$\dot{\rho}(\mathbf{r}, t) = \nabla \cdot \overleftrightarrow{D} \nabla\rho(\mathbf{r}, t) + \nabla \cdot \overleftrightarrow{D} \nabla \left[(k_B T)^{-1} V(\mathbf{r}, t) - (\hat{C}_0 - \sum_{i,j=1}^{d} a_{ij}\frac{\partial^2}{\partial x_i \partial x_j} + \sum_{i,j,k,l=1}^{d} b_{ijkl}\frac{\partial^4}{\partial x_i \partial x_j \partial x_k \partial x_l})\rho(\mathbf{r}, t) \right]. \tag{25}$$

If one further uses the constant mobility approximation, $\rho(\mathbf{r}, t) = \rho$ in front of the functional derivative in eq. (17) and if one approximates

$$F_{\mathrm{id}}\left[\rho(\mathbf{r})\right] \approx k_B T\rho \int \mathrm{d}\mathbf{r} \left\{ \frac{1}{2}\phi(\mathbf{r}, t)^2 - \frac{1}{6}\phi(\mathbf{r}, t)^3 + \frac{1}{12}\phi(\mathbf{r}, t)^4 - \mathrm{const.} \right\} \tag{26}$$

with $\phi(\mathbf{r}, t) = \Delta\rho(\mathbf{r}, t)/\rho$, one arrives at:

$$\dot{\phi}(\mathbf{r}, t) = \rho\nabla \cdot \overleftrightarrow{D} \nabla \left[\phi(\mathbf{r}, t) - \frac{1}{2}\phi(\mathbf{r}, t)^2 + \frac{1}{3}\phi(\mathbf{r}, t)^3 + (k_B T)^{-1} V(\mathbf{r}, t) - \rho(\hat{C}_0 - \sum_{i,j=1}^{d} a_{ij}\frac{\partial^2}{\partial x_i \partial x_j} \right.$$

$$\left. + \sum_{i,j,k,l=1}^{d} b_{ijkl}\frac{\partial^4}{\partial x_i \partial x_j \partial x_k \partial x_l})\phi(\mathbf{r}, t) \right]. \tag{27}$$

This exactly reduces to the anisotropic phase-field model of ref. [23] for the special case $d = 2$, $\overleftrightarrow{D} = D_0\overleftrightarrow{1}$, and a neglected cubic term in the ideal gas functional expansion in eq. (26). As a remark the latter was retained in other variants of the PFC model [17,44].

Concluding this section, the anisotropic phase-field crystal model as used in [23] can be derived and justified from dynamical density functional theory. The derivation points, however, to more realistic approximations for anisotropic diffusivities. Furthermore, if eq. (26) is used, some approximations can be avoided but these were not found to change the results significantly for spherical interactions [21].

3.1 Phenomenological symmetry considerations

We now present phenomenological symmetry arguments for the expansion coefficients a_{ij} and b_{ijkl} of the anisotropic PFC model. First we assume that the orientation of the fixed particles is set by a single unit vector $\boldsymbol{E}$ only which is invariant under space inversion ($\boldsymbol{r} \to -\boldsymbol{r}$). This is the case for $d = 2$ and for rotationally symmetric particles in $d = 3$. Then, any gradient term in the scalar free energy functional must involve an even number of gradients due to space inversion symmetry. Rotational symmetry of space then requires that only combinations of $\boldsymbol{E} \cdot \boldsymbol{\nabla}$ and $\boldsymbol{\nabla} \cdot \boldsymbol{\nabla}$ are nonvanishing in the functional. Therefore the only possibility for physically relevant gradient terms is

$$\sum_{i,j=1}^{d} a_{ij} \frac{\partial^2}{\partial x_i \partial x_j} = \lambda_1 (\boldsymbol{E} \cdot \boldsymbol{\nabla})^2 + \lambda_2 \Delta, \tag{28}$$

and

$$\sum_{i,j,k,l=1}^{d} b_{ijkl} \frac{\partial^4}{\partial x_i \partial x_j \partial x_k \partial x_l} = \lambda_3 (\boldsymbol{E} \cdot \boldsymbol{\nabla})^4 + \lambda_4 (\boldsymbol{E} \cdot \boldsymbol{\nabla})^2 \Delta + \lambda_5 \Delta^2, \tag{29}$$

where λ_1, λ_2, λ_3, λ_4, and λ_5 are scalar prefactors. This reduces the number of independent degrees of freedom in a_{ij} and b_{ijkl} down to 5.

In the case of different fixed vectors, say $\boldsymbol{E}$ and $\boldsymbol{B}$, there are corresspondingly more terms allowing for more freedom in a_{ij} and b_{ijkl}. This is realized, *e.g.*, for biaxial colloidal particles in two crossed external fields along $\boldsymbol{E}$ and $\boldsymbol{B}$.

4 Extensions, generalizations and refinements of the concept

In this article, our special focus is on such extensions of the phase-field crystal method, which are aiming particularly at capturing realistic phase diagrams more and more accurately. For clarity purpose we thereby restrict our focus to the "one-mode" to "two-mode" to "eighth-order–fitting version" route that can be found as main route in the literature. To understand this main route of PFC extension for the above purpose let us start again with the simplest phase-field crystal model given by the Swift-Hohenberg model equation above. If one compares this simplest form of the PFC model with classical density functional theory (DFT), it is based on the same idea of representing the free energy of a material by a functional of its density [43,45,46,28,47–49]. The precise functionals employed, however, differ due to the fact that the DFT methods seeks a most realistic mean-field description of the crystal density field $n(\boldsymbol{r})$ with aim to reproduce quantitatively as accurately as possible the properties of a material [50]. Expressing $n(\boldsymbol{r})$ as expansion of the following form:

$$n(\boldsymbol{r}) = n_0 \left(1 + \sum_i u_i e^{i\boldsymbol{K}_i \cdot \boldsymbol{r}} \right), \tag{30}$$

where each $\boldsymbol{K}_i$ represents a different reciprocal lattice vector, this implies taking into account a large number of terms of the expansion. On the contrary, PFC models consider much lesser terms in the expansion to be able to simulate larger time and length scales of materials evolution. Now the Brazovskii/Swift-Hohenberg–based [22], PFC approach with the free energy functional (12) is in the end a one-mode model truncating eq. (30) to one set of RLVs with equal magnitude $|\boldsymbol{K}_i| = q_0$ [50]. The price paid is that only a small number of crystal structures can be modeled with that kind of one-mode PFC model (see sect. 5 for further details). This motivated the authors of [50] to extend model (12) to a *two-mode* phase-field-crystal model based on the following free energy density:

$$f = \frac{\phi}{2} \left[a + \lambda (\nabla^2 + q_0^2)^2 ((\nabla^2 + q_1^2)^2 + r_1) \right] + u \frac{\phi^4}{4}. \tag{31}$$

This model truncates eq. (30) to two sets of RLVs, one with magnitude $|\boldsymbol{K}_i| = q_0$ and one with $|\boldsymbol{K}_i'| = q_1$. Even though the new model (31) has so far only been demonstrated to produce stability domains for fcc and bcc phases, one gain of the model is that it can produce fcc structure close to the critical point, *i.e.* in the regime of linear elasticity.

The free energies of the one-mode and two-mode PFC models can be re-cast into a unified form in terms of the parameter $\lambda = R_1/(1+R_1) \in [0,1]$ (R_1 is the relative strength of the first- and second-mode contributions [50]), which can be used to interpolate between the 2M PFC ($\lambda = 0$) and 1M PFC ($\lambda = 1$) models:

$$\mathcal{F} = \int d\mathbf{r} \left\{ \frac{\psi}{2} \left[-\epsilon + (1 + \nabla^2)^2 \times (\lambda + \{1 - \lambda\} \{Q_1^2 + \nabla^2\}^2) \right] \psi + \frac{\psi^4}{4} \right\}, \tag{32}$$
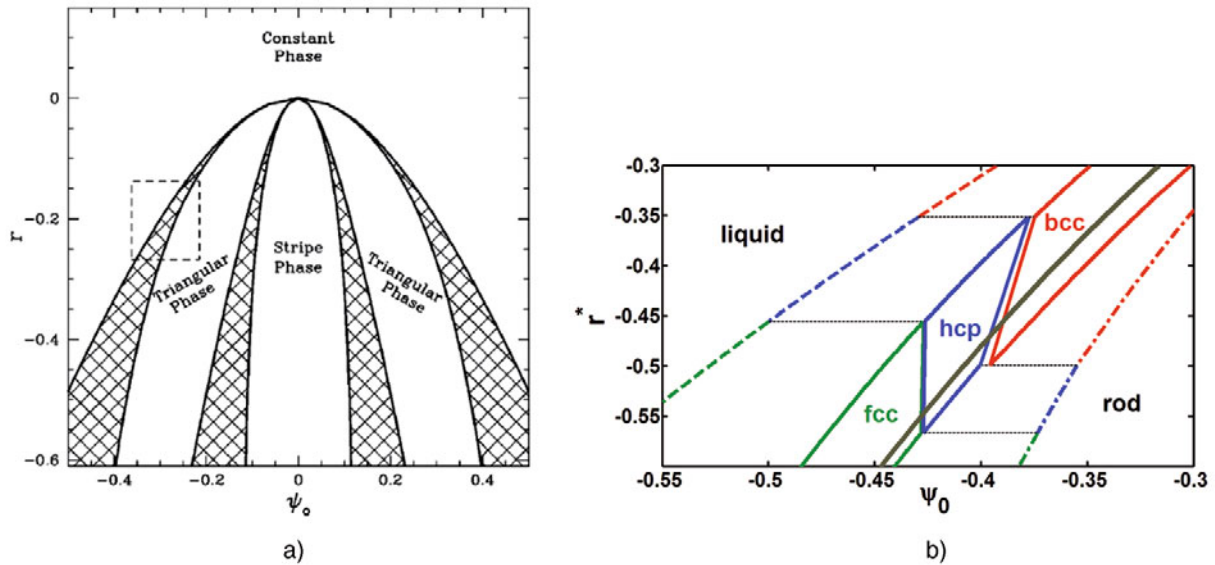
Fig. 2. (a) Single-mode approximation to the phase diagram of the 1M PFC model in 2D [15]. (b) Section of the 3D phase diagram of 1M PFC model evaluated by the Euler-Lagrange method described in [51]. Note the stability domains of the bcc, hcp, and fcc phases. The liquid is unstable to the right of the heavy gray line. Here $\epsilon = |r^*|$.

where $\psi \propto (\rho - \rho_L^{ref})/\rho_L^{ref}$ is the scaled density difference relative to the reference liquid of particle density ρ_L^{ref}. The reduced temperature $\epsilon \propto a$ can be related to the bulk moduli of the fluid and the crystal, whereas $Q_1 = q_1/q_0$ $(= 2/3^{1/2}$ for fcc [50]) is the ratio of the wave numbers corresponding to the two modes.

An improved representation of real bcc materials has been achieved by Jaatinen *et al.* [52] in another extension of the 1M PFC approach that they call the eighth-order–fitting model (EOF). This model reproduces a range of thermodynamic properties of pure iron (including the anisotropy of the solid-liquid interface free energy) owing to the extra model parameters emerging from a higher-oder expansion of the direct correlation function, which ensure a higher degree of flexiblity.

A still different approach obtained by the introduction of an anisotropic tensor in the free energy functional, was motivated and outlined above in sect. 3. The implications of these model extensions with respect to phase diagrams, nucleation and pattern formation are illustrated in the following sect. 5.

5 Phase diagrams, nucleation and pattern formation

5.1 Phase diagrams

The different versions/extensions of the PFC model, reviewed in sect. 4, have been designed to prefer different crystal structures; hence they lead to different phase diagrams, whose form in turn depends on the dimensionality of the system. In 2D and 3D, the 1M PFC (the original theory by Elder *et al.* [15]) leads to the phase diagrams shown in fig. 2. In 2D, a single crystalline phase appears (the triangular phase) that coexists with the liquid and a striped phase [15]; whereas in 3D, both full thermodynamic optimization [52] and an equivalent method relying on solving the Euler-Lagrange equation [51], identifies stability domains for the bcc, fcc, and hcp structures. Apparently, the 1M PFC model prefers the formation of the bcc phase near the critical point. In contrast, the 2M PFC model of Wu *et al.* designed to realize fcc crystallization [50], suppresses the bcc phase (fig. 3(a)). The 2M PFC model incorporates the 1M PFC model as a limiting case. Interpolation between 1M PFC and the fully fcc limit ($R_1 = 0$), in terms of the parameter R1 leads to the appearance of a bcc stability domain in the vicinity of the critical point (fig. 3(b)). (R_1 is the ratio of the Fourier amplitudes for the density waves having the second and first neighbors RLVs as wave vector.) Whether this is accompanied with the appearance of an hcp stability domain, as in the 1M PFC limit, is yet unclear.

The applicability of the EOF PFC model has been demonstrated for Fe [44]. The free energy *vs.* particle density curves for the solid and liquid phases, which were used to determine the equilibrium conditions at the melting point, are shown in fig. 4. No phase diagram has been published for this model. It appears that much like the original the 1M PFC model, it prefers bcc freezing.

Another attempt to control the preferred crystal structure manipulates the two-particle direct correlation function so that its peaks prefer the desired structural correlations [53]. The phase diagram and the respective free energy curves
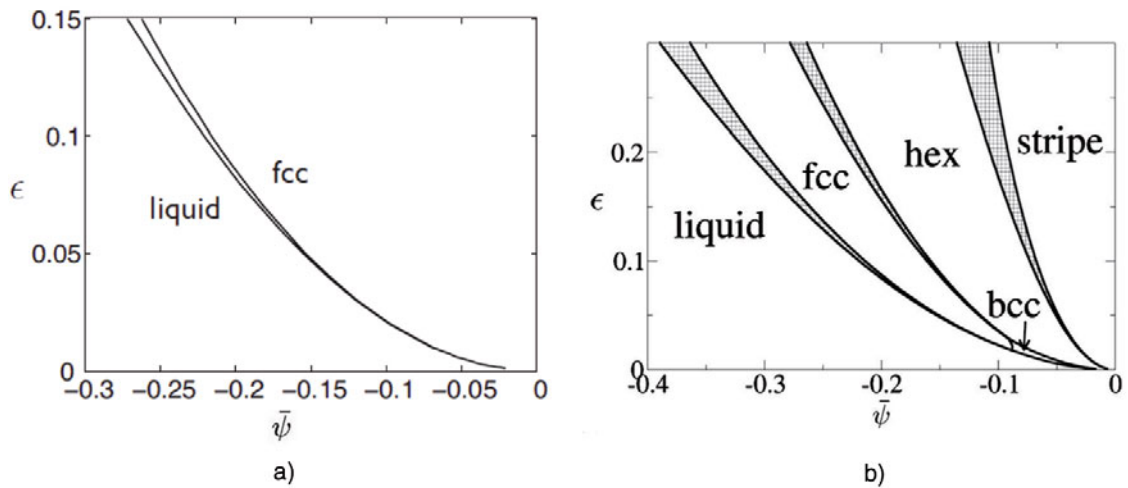
Fig. 3. (a) Single-mode approximations to the phase diagram of the 2M PFC model in 3D for $R_1 = 0$ [50]. (b) The same for $R_1 = 0.05$. Note the small bcc stability domain near the critical point.
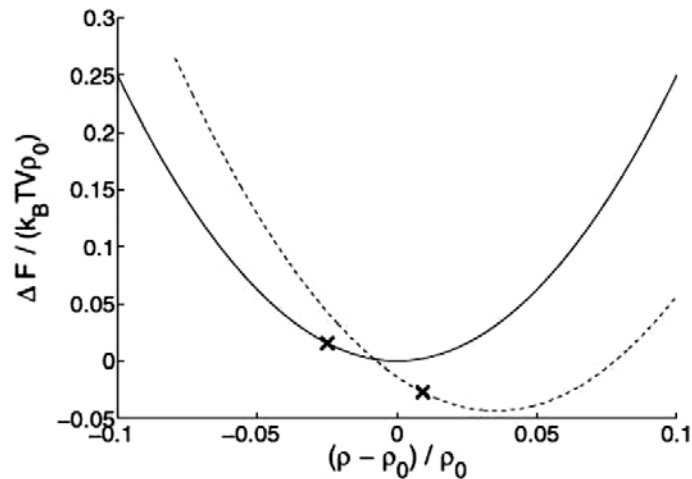
Fig. 4. Free-energy density for the liquid (solid) and bcc (dashed) Fe as a function of reduced particle density at the melting point in the EOF PFC model [44]. Crosses denote the equilibrium points obtained by the common tangent method.

are shown for a case that forces coexistence between the bcc and fcc structures (fig. 5). The binary generalization of the 1M PFC model in 2D has been presented in detail by Elder *et al.* [17]. The phase diagram of a binary system that shows eutectic solidification is shown in fig. 6. The 3D extension of this approach has been investigated by Tóth *et al.* [51]. The map of thermodynamic driving force for solidification as a function of composition and density of the initial liquid is shown in fig. 7. 3D eutectic solidification has indeed been observed in the domain of the largest driving force.

One of the most intriguing questions is how to extend the PFC framework to accommodate the properties of real materials including alloys. A binary extension of the EOF PFC model might be worth exploring.

5.2 Crystal nucleation in 2D and 3D

Crystal nucleation can be handled in two ways within the framework of PFC models: i) Via finding the properties of the critical fluctuations (nuclei) by locating the respective solutions, which extremize the free energy functional; ii) by adding noise to the equation of motion. Both approaches have their limitations. i) is expected to work for small undercoolings, where the individual heterophase fluctuations do not interact. Furthermore, it is not immediately straightforward how one should address possible non-crystalline nucleation precursors. In turn, in the case of ii) it is not clear conceptually, which fraction of the thermal fluctuations is already integrated into the free energy, and which wavelengths should yet be added (see, *e.g.*, [54,55] and the discussion in [56,57]) as noise to the equation of motion; a question inherently related to the proper choice of the high-frequency cut-off one needs to make to avoid an
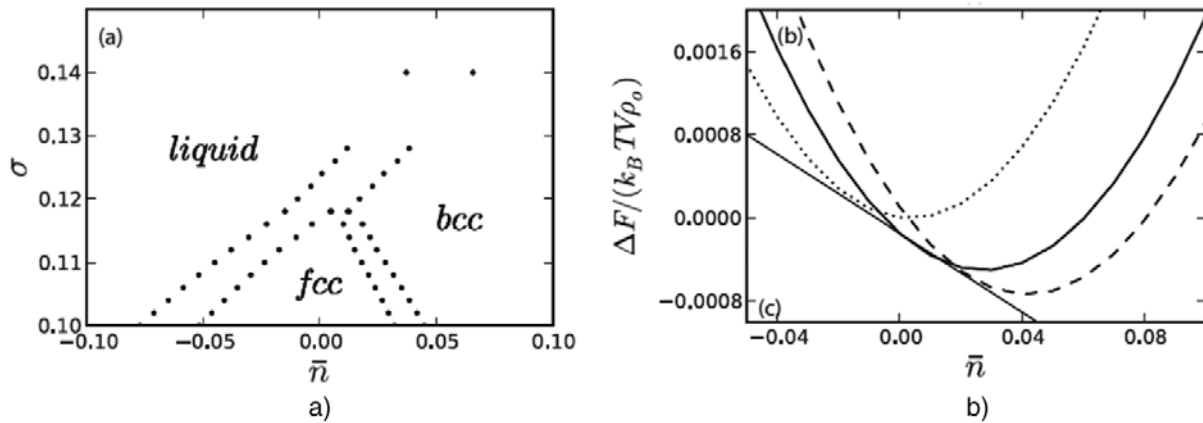
Fig. 5. (a) Phase diagram for a system whose direct correlation function was manipulated so that coexistence between the fcc and bcc structures is realized [53]. (b) Free energy *vs.* reduced density near the peritectic temperature in the same model.
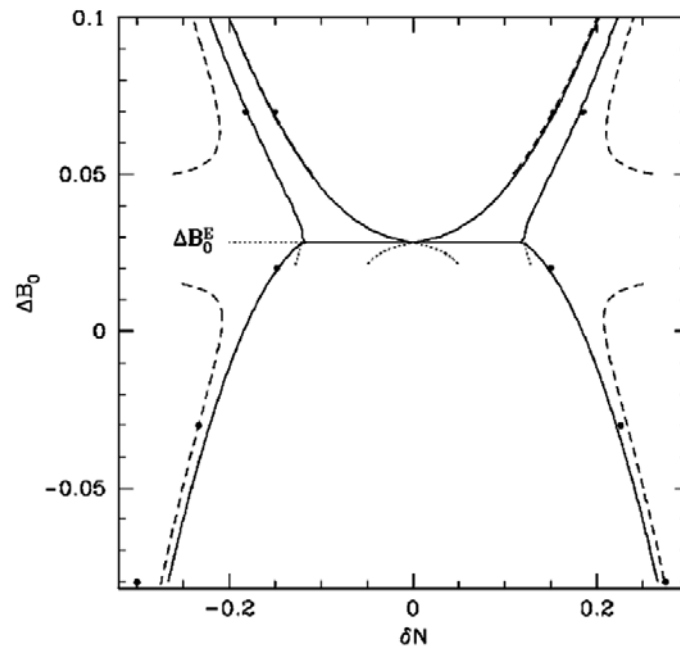
Fig. 6. Phase diagram for the binary 1M PFC model in 2D [17], as a function of parameters related to the undercooling (ΔB_0) and to the chemical composition (δN). In the appropriate range indeed eutectic solidification has been observed with both solid phases having a triangular structure.

ultraviolet catastrophe in 3D. Furthermore, the addition of noise to the equation of motion changes the free energy, the phase diagram, and the interfacial properties. While, in principle, correction of these is possible via parameter renormalization [58,59], further study is needed in the case of PFC models.

On the other hand, the original free energy functional used in i) seems to miss the effect of longer wavelength fluctuations, which could move the system out of a metastable state. Considering these, i) and ii) may be considered as the approaches that provide complementary, probably qualitative information of the crystallizing system. First, we review results obtained following route i).

5.2.1 Properties of the critical fluctuations

a) *Homogeneous nucleation* – An adaptation of the string method to find the saddle point of the free energy functional has been used by Backofen and Voigt [60] for determining the properties of the critical fluctuations in the 1M PFC model in 2D. The respective density profiles are shown in fig. 8. It is evident that at large supersaturations there are
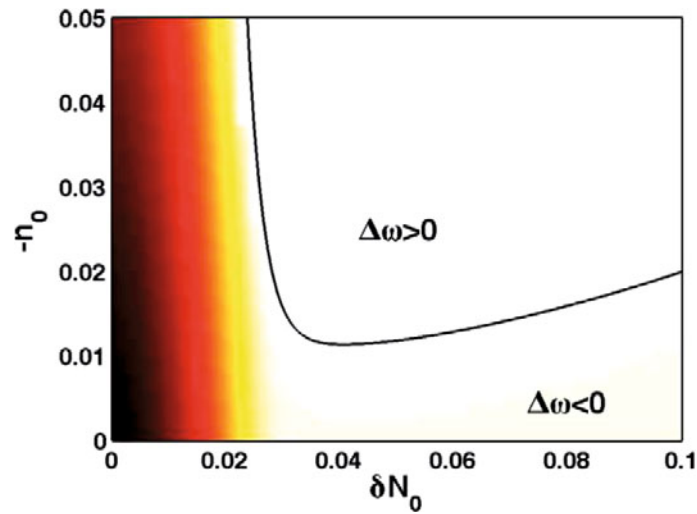
Fig. 7. Color map for the driving force of eutectic solidification (grand potential density difference relative to the liquid) for the binary 1M PFC model in 3D [51], as a function of density (n_0) and the chemical composition (δN_0). Note that solidification is expected in the region where $\Delta\omega < 0$.
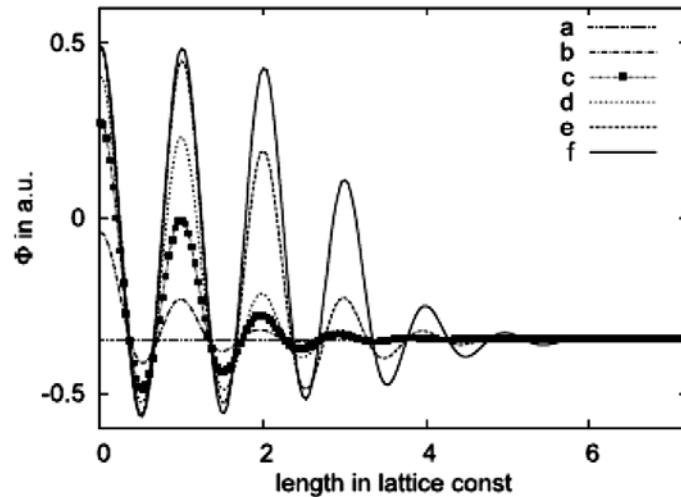
Fig. 8. Particle density profiles for the critical fluctuations forming at different supersaturations (supersaturation increases from f to a), as obtained by the adaptation of string method for the 1M PFC model in 2D [60].

no bulk crystal properties at the center of the smallest nuclei. They have also reported that small nuclei are faceted even though the large crystals are not.

Tóth *et al.* [51] have solved the Euler-Lagrange equation for the appropriate boundary conditions (homogeneous supersaturated liquid in the far field), to find the free energy extrema far from the critical point ($\epsilon = 0.5$) for the 1M PFC model in 2D, where even the large crystals are inherently faceted. It has been found that the free energy surface has many local minima that map out the shape of the free energy barrier for nucleation as a function of size (fig. 9). The effective interfacial free energy evaluated from the barrier height converges towards the free energy of the planar interface as the supersaturation decreases.

A similar analysis has been performed in 3D by Tóth *et al.* [51] to study heterophase fluctuations in the 1M PFC model. They have determined the properties of crystal nuclei for bcc and fcc structures. It has been found that, under the investigated conditions, both the nucleation barrier and the driving force are fairly close for the two structures implying comparable interfacial free energies.

b) *Heterogeneous nucleation* – Tóth *et al.* used a periodic external potential to incorporate crystalline substrate into the Euler-Lagrange method for determining the properties of faceted heterogeneous nuclei [51]. They have observed the adsorption of a monolayer of particles on the surface of substrate that reduced the formation energy of nuclei substantially, and lead to a contact angle of 60 deg. determined by the crystal structure. Further studies aimed at determining the role played by lattice mismatch, crystal structure, etc. are yet required.
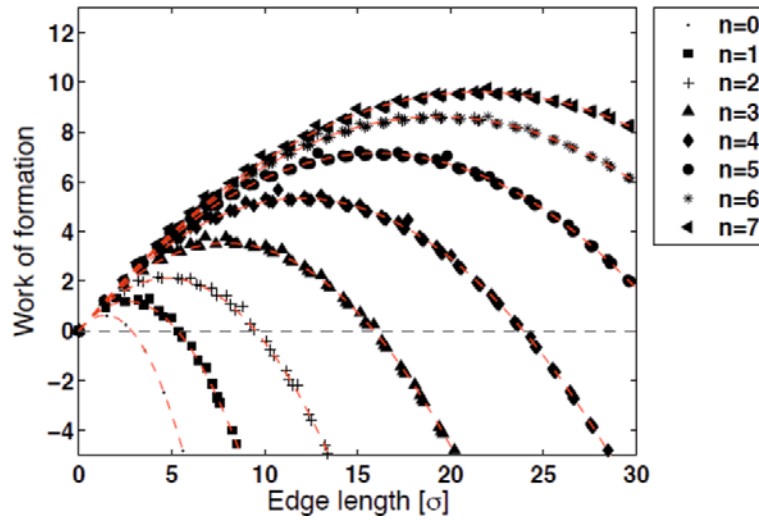
Fig. 9. Nucleation barrier *vs.* size relationship for homogeneous crystal nuclei with faceted interfaces in the 1M PFC model as obtained by solving the Euler-Lagrange equation at $\epsilon = 0.5$ and $\psi_0^n = -0.5134 + 0.0134/2n$, where $n = 0, 1, 2, \ldots, 7$, respectively [51].
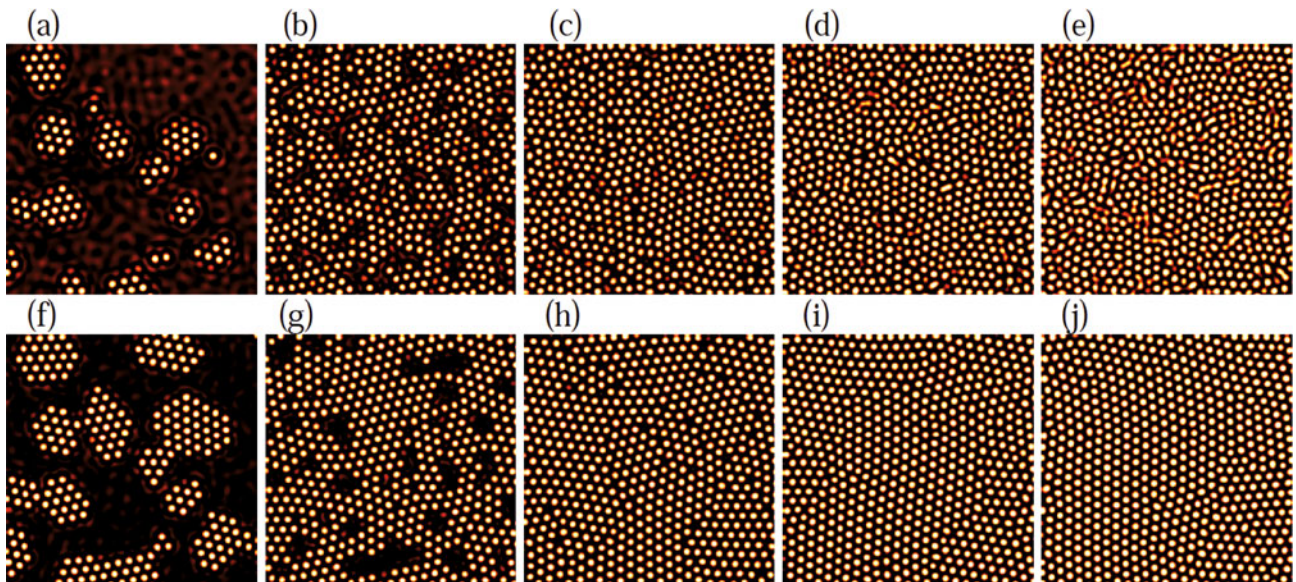
Fig. 10. Snapshots of early and late stages of isothermal solidification in 1M PFC simulations performed in 2D with initial reduced particle densities of $\psi_0 = -0.55, -0.50, -0.45, -0.40$ and -0.35 [66]. (a)–(e) Early stage: the respective reduced times are $250, 75, 37.5, 25$, and 17.5. (f)–(j) Late stage: the same areas are shown at reduced time 1500. (418×418 fractions of 2048×2048 sized simulations are shown. Other simulation parameters were: $\epsilon = 0.75$ and (noise strength) $\alpha^* = 0.1$. Reduced particle density maps are shown.)

5.2.2 Simulation of crystal nucleation

a) *Homogeneous nucleation* – A systematic study of the effect of the noise strength on the grain size distribution has been performed by Hubert *et al.* [61] for the original PFC model in 2D. Freezing of undercooled liquids often starts with the nucleation/formation of metastable phases. Mounting theoretical and experimental evidence shows that even in the simplest systems (including the Lennard-Jones and hard-sphere model systems, and 2D and 3D colloidal suspensions) a dense liquid/amorphous precursor precedes the nucleation of the crystalline phase [62–65].

The PFC methods have been used to explore this behavior both in 2D and 3D [51,66]. In 2D, it has been shown within the framework of the 1M PFC model that at relatively small supersaturations direct crystal nucleation takes place. Increasing the thermodynamic driving force, first copious crystal nucleation is observed, and at higher driving forces an amorphous precursor precedes crystalline nucleation [66] (fig. 10). Interestingly, similarly to experiments for

2D colloidal systems [67], no hexatic phase is observed in the 1M PFC simulations (as proven by the form of the radial decay of the bond-order correlation function [66]).

Similar behavior has been reported for bcc nucleation in compressed Fe melt in 3D in the framework of the EOF PFC model [51,66]. Here the initial density of the liquid has been increased until the solidification started. For this, an enormous compression was needed owing to the small size and time scale accessible for the simulations. This raises doubts whether the applied approximations are still valid, nevertheless, the behavior observed for the EOF PFC Fe is fully consistent with the results obtained for the 1M PFC model while reducing the temperature (ϵ). With increasing driving force first an amorphous precursor nucleates, and the bcc phase appears inside these amorphous regions [51] (fig. 11). At higher driving forces the amorphous precursor appears simultaneously in space and the bcc phase nucleates later. Apparently, direct nucleation of the bcc phase requires a longer time than were accessible for these PFC simulations, suggesting that the appearance of the bcc phase is assisted by the presence of the amorphous phase, in line with recent predictions by the density functional theory [62] and atomistic simulations [65].

Remarkably, the amorphous matter appearing in these simulations via nucleation (which suggests a first-order phase transition) seems to coexist with the liquid phase at least in certain parts of the phase diagram of the 1M PFC model, so this amorphous matter might indeed be different from the usual kinetically arrested amorphous phase. Interestingly, such coexistence has been reported for empirical model potentials developed for metallic systems (Adams-Ercolessi potential for Al [68]). The physical ground for the preference for the amorphous precursor requires further investigation. Recently, Tóth *et al.* [51] raised the possibility (on the basis of an effective pair potential they evaluated from the structural data for the amorphous phase) that the interaction potential has a peak at $r_0\sqrt{2}$, where r_0 is the radius for the main minimum for the attractive part, which would then disfavor the close-packed order usually favored in monatomic systems [69].

b) *Heterogeneous nucleation* – Prieler *et al.* [23] have explored crystal nucleation on unstructured hard wall in an anisotropic version of the 1M PFC model, in which the particles are assumed to have an ellipsoidal shape. In particular, they have investigated how the contact angle depends on the orientation of the ellipsoids and the strength of the wall potential (fig. 12). A complex behavior has been observed for the orientation dependence, while increasing the strength of the wall potential reduced the contact angle.

Gránásy *et al.* [66] have studied crystal nucleation in rectangular corner of structured and unstructured substrates within the 1M PFC model in 2D. Despite expectations based on the classical nucleation theory, which predicts that a corner should be a preferred nucleation site, owing to the misfit of the triangular crystalline structure with a rectangular corner, in the atomistic approach this corner is not a preferable site of nucleation (fig. 13).

5.3 Pattern formation

Owing to the diffusive dynamics, the equation of motion chosen to describe the time evolution of the particle density in the PFC models enforces, diffusional instabilities that lead to fingering of the growing crystal front are inherently incorporated. This being so, whether a single component or a binary version is considered: In the case of a single-component PFC model, diffusive dynamics means that as the growing crystal (of larger particle density than the liquid) consumes the particles in the adjacent liquid, the only way they can be replenished is via long range diffusion form the bulk liquid. Accordingly a depletion zone forms ahead of the growing crystal. This resembles the behavior of colloidal suspensions, in which the micron sized colloid particles move by Brownian motion in the carrier fluid. Relying on this similarity, the single component PFC models can be considered as reasonable tools to address colloidal crystal aggregation. Similar conditions might occur on the surface of substrates, where the adsorbed particles may move by diffusion in a periodic potential field. 2D PFC models can be used to capture pattern formation due to the interplay of the inter-particle forces and the periodic potentials representing the symmetries of the substrate.

5.3.1 Pattern formation in single-component PFC

a) *Ordering on substrate surfaces* – Achim *et al.* [70] and Ramos *et al.* [71] have used periodic (pinning) potentials in the PFC model to represent the effect of a periodic substrate on the surface layer. They have explored commensurate-incommensurate transitions as a function of the strength of the pinning potential and the lattice mismatch using a two-mode (hexagonal-square) ansatz and numerical simulations (see fig. 14).

b) *Pattern formation in 2D colloidal systems* – choosing a suffucuently large value for the parameter ϵ, where the solid-liquid interface is faceted, Tegze *et al.* [72,73] have investigated solidification morphologies as a function of the thermodynamic driving force. It has been found that the diffusion controlled growth mode observed at low driving forces and is characterized by faceted interfaces changes to a diffusionless growth mode of a diffuse solid-liquid interface that produces a crystal whose density is comparable density to the density of the liquid due to quenched-in vacancies. This "density trapping" phenomenon is analogous to the solute trapping observed in rapid solidification of alloys, where due to lack of time for partitioning solids of non-equilibrium compositions form. These two modes have
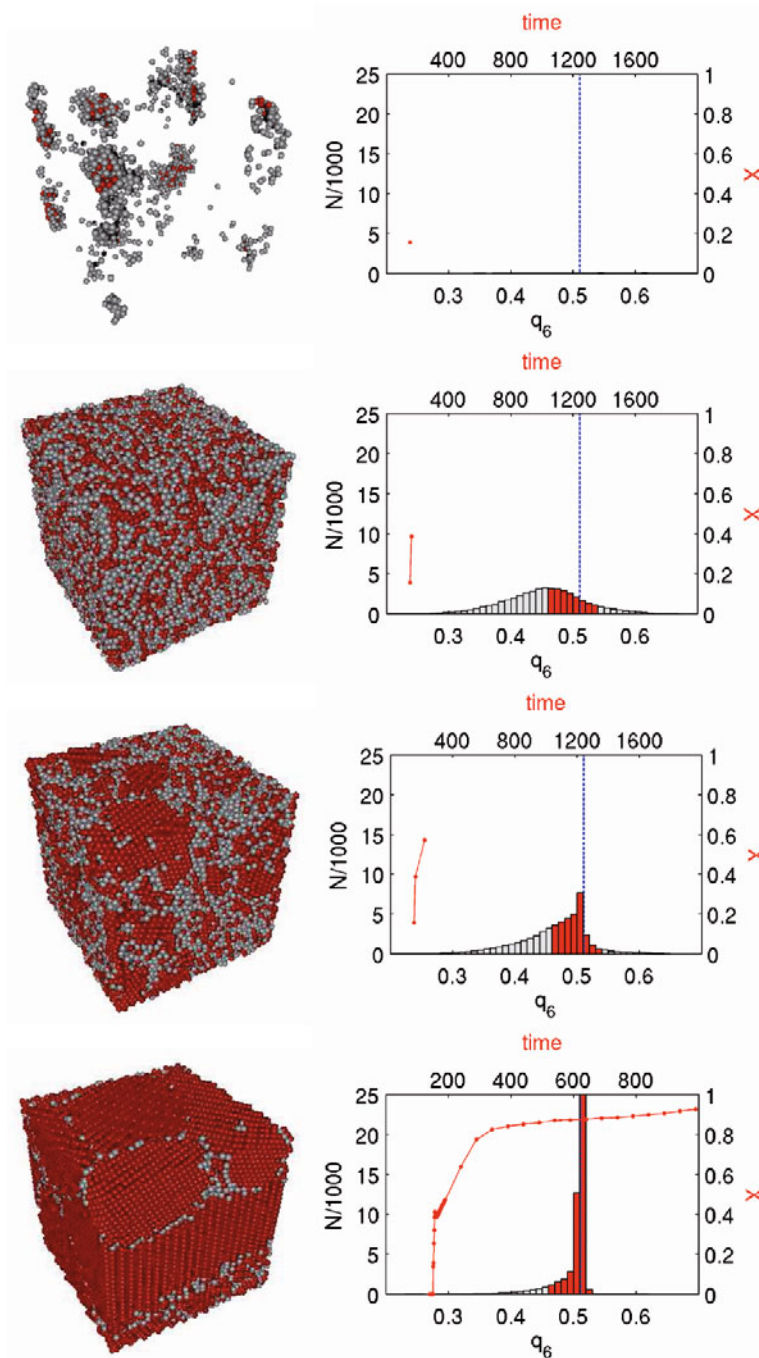
Fig. 11. Crystal nucleation in compressed Fe liquid in the EOF PFC model [51]. Snapshots taken at four instances (from top to bottom, the dimensionless time is $t = 153, 160, 220$, and 990). Circles drawn around density peaks are shown on the left. The "particles" are colored in red if they have a bcc-like neighborhood according to a structural analysis performed in terms of the q_6 order parameter. Histograms showing the probability distribution for q_6 and the time dependence of the bcc-like fraction (X) are presented on the right. The blue vertical line shows the q_6 value corresponding to the ideal bcc structure.

already been observed experimentally in colloidal systems [74]. It has been shown that the two modes can coexist and lead to a new branching mechanism that differs from the usual diffusional instability driven branching that leads to the formation of dendritic structures. This new mechanism explains the fractallike and porous growth morphologies observed in 2D colloidal systems (fig. 15), and may be relevant for the diffusion controlled to diffusionless transition of crystallization in organic glasses.
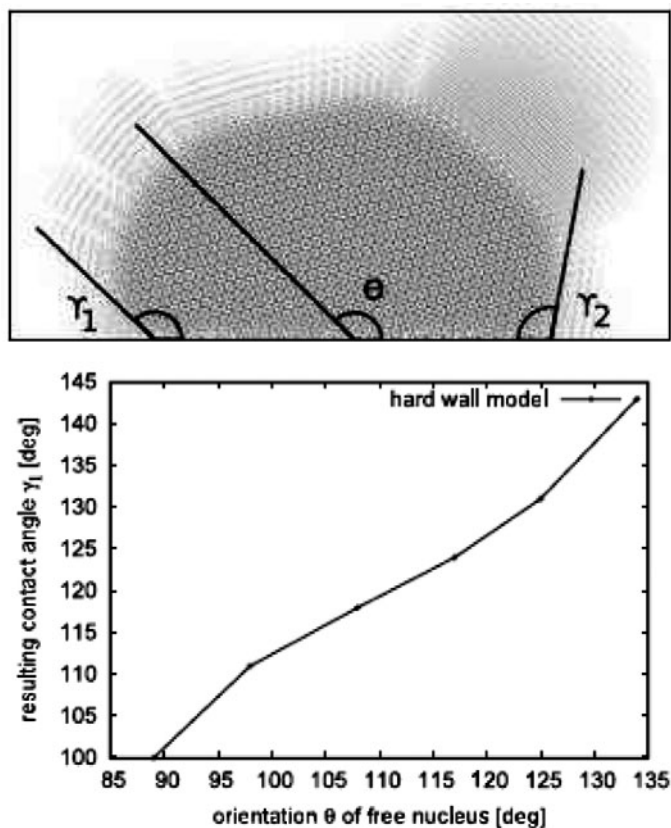
Fig. 12. Heterogeneous nucleation in an anisotropic version of the 1M PFC model in 2D [23]. The dependence of the contact angles (γ_1 and γ_2) on the orientation Θ of the ellipsoidal molecules relative to the hard wall is represented by a wall potential.
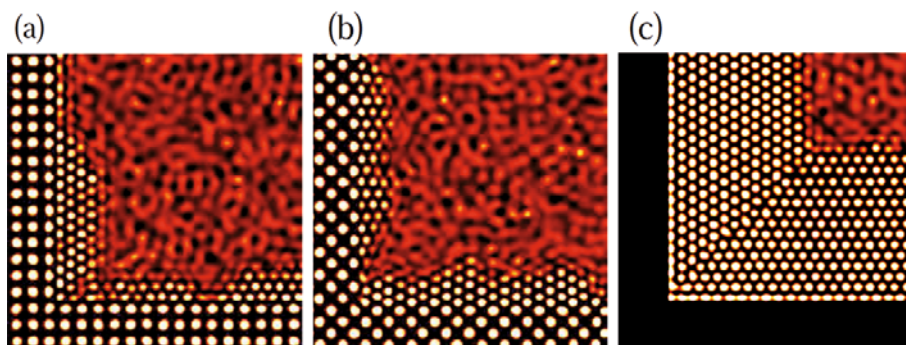
Fig. 13. Heterogeneous nucleation in rectangular inner corners of the 1M PFC model in 2D [66]: (a) on (01) surfaces of a square lattice (ratio of lattice constant of substrate to interparticle distance $a_0/\sigma \approx 1.39$); (b) on (11) surfaces of a square lattice; and (c) on an unstructured substrate. Note the frustration at the corner and the formation of a grain boundary starting from the corner at later stages.
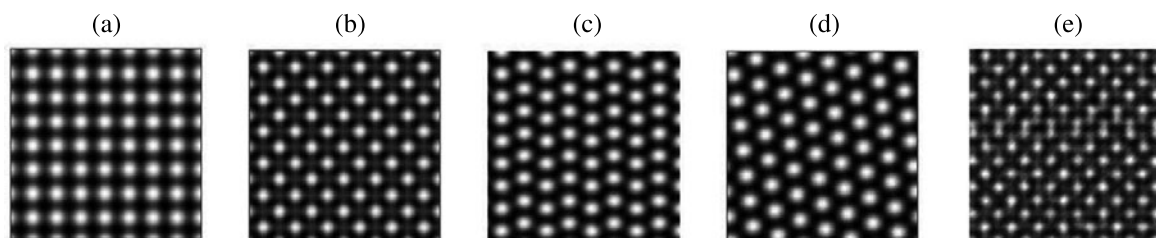
Fig. 14. Particle density maps showing commensurate (a)-(c) and incommensurate (d) and (e) structures in the ground state, obtained by varying the strength of the pinning potential and the misfit [71].
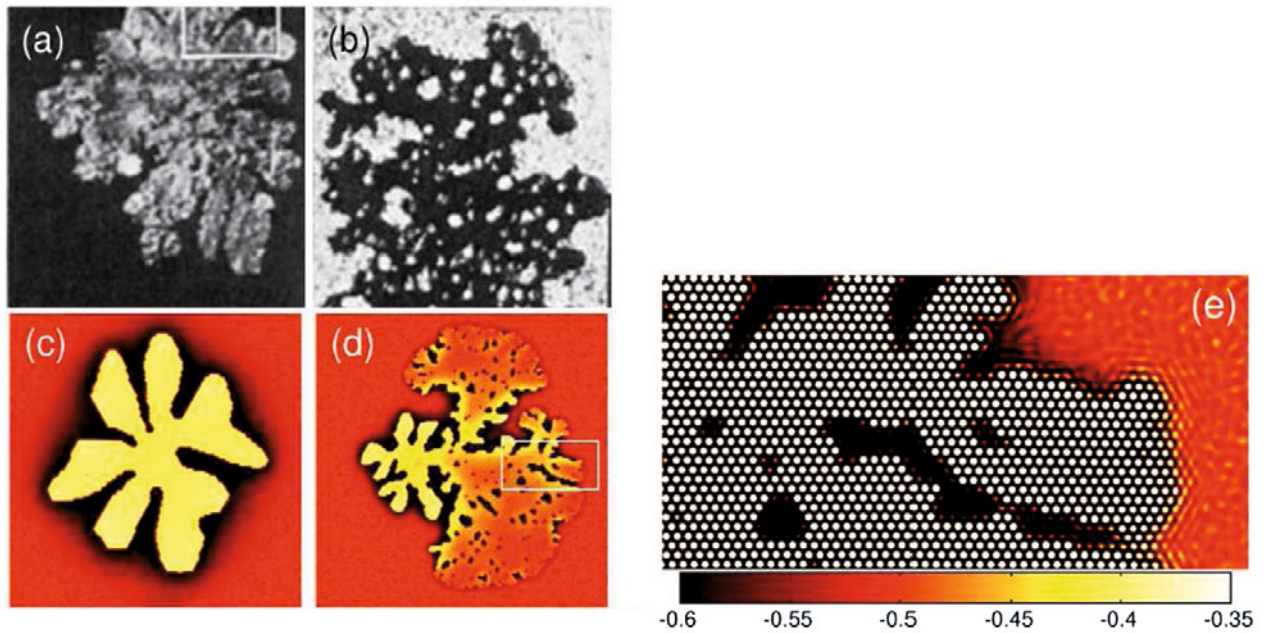
Fig. 15. Dendritic ((a),(c)) and fractal-like/porous single-crystal growth forms ((b),(d)) in the experiments ((a),(b)) and 1M PFC simulations ((c)-(e)) [73]. While the growth of the dendritic structure is governed by the diffusion field around it (see the depletion zone around the crystal), the fractal-like/porous growth forms on the right have slow interfaces growing under diffusion control and fast interfaces traveling with a constant velocity. A close-up of the interface is shown in (d) for "fast" mode: extended structural ordering on the liquid side and "slow" mode: sharp interface with deep depletion zone ahead.

Fig. 16. Dendritic and eutectic growth in 2D (first row [75]; second row [76] and [51]) and 3D (third row: bcc and fcc dendrites [51], and bcc eutectics [51]) in the binary 1M PFC model.
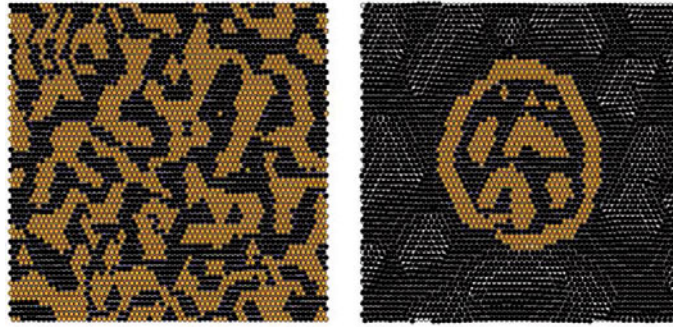
Fig. 17. PFC simulation for CoAg alloy formation on Ru (0001) substrate [77]. Black and yellow circles represent Ag and Co atoms, whereas the empty circles stand for hcp sites on the Ru (0001) surface. Left: pseudomorphic nanoscale alloy for equal composition. Right: Ag-rich system.
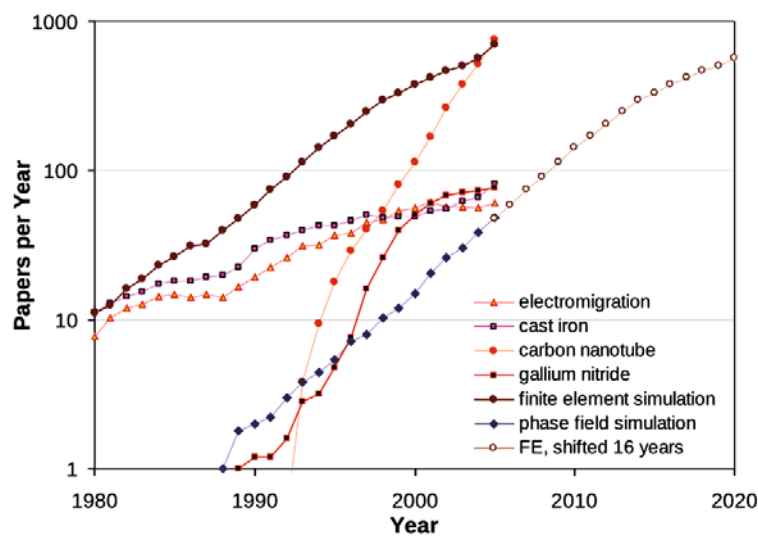
Fig. 18. The figure provides on outlook on the possible further development of phase-field–based research in materials science measured by the number of published papers. In this form it was given by H. Assadi in 2004 [83], arriving at a curve similar to that for FEM just shifted by 16 years. If this curve can simply be shifted by another 14 years to show the development of phase-field-crystal–based work in materials science will depend to a large extend on the question on how it will become possible to model the multitude of different phase diagrams in materials science even more accurately, *i.e.* going beyond what has been discussed with respect to that issue in sects. 4 and 5 of this article. Figure kindly provided by Hamid Assadi.

5.3.2 Pattern formation in binary PFC models

Dendritic and eutectic solidification have been addressed in the binary version of 1M PFC model by Elder *et al.* [17] in 2D [51,17,75,76] and 3D [51] (fig. 16). It has been shown that in the PFC model, binary eutectic solidification may lead to the formation of eutectic colonies due to the diffusive dynamics applying to the total number density [51].

Muralidharan and Haataja [77] have extended 1M PFC model for describing stress induced alloying of bulk-immiscible binary systems on substrate by adding a potential energy term describing the substrate and a regular solution term. Fixing the model parameters to data for CoAg/Ru(0001), they demonstrated that the model captures experimentally observed morphologies (fig. 17).

6 Summary and outlook

In this article we have introduced the phase-field crystal method in comparison to the phase-field method. Further we have reviewed basic steps in its generalization and further development to become a more and more comprehensive tool to capture realistic materials' phase-diagrams, nucleation and pattern formation. Certainly these have not been the only applications of the phase-field crystal method in materials science over the past decade: for other applications

such as simulations of features of crack propagation [17] and plasticity [16,78] from the atomic to the micro-scale, protein crystals in a membrane [79], or liquid crystals [80–82] we refer the reader to the just provided literature and references therein.

Here we would like to conclude with an outlook, which we relate to an outlook that was given by H. Assadi in a talk 2004 on the phase-field method. In it he compared the development of phase-field based research to other fields of materials science and extrapolated it to the year 2020 ariving at a curve quite similar of that for FEM just shifted by 16 years [83] as depicted in fig. 18. If this curve can simply be shifted by another 14 years to show the development of phase-field *crystal* method based work in materials science will depend to a large extend on the question in how far it will become possible to model the multitude of different phase-diagrams in materials science still more quantitatively, *i.e.* going beyond what has been discussed with respect to this issue in sects. 4 and 5 of this article.

References

1. For a monograph see: H. Emmerich, *The Diffuse Interface Approach in Material Science - Thermodynamic Concepts and Applications of Phase-Field Models*, Lect. Notes Phys. Mon., Vol. **73** (Springer, Berlin, 2003).
2. L.Q. Chen, Annu. Rev. Mater. Res. **32**, 113 (2002).
3. W.J. Boettinger, J.A. Warren, C. Beckermann, A. Karma, Annu. Rev. Mater. Res. **32**, 163 (2002).
4. For a recent review summarizing the advances of and by phase-field modeling in condensed matter physics, see: H. Emmerich, *Advances of and by phase-field modeling in condensed matter physics*, Adv. Phys. **57**, 1 (2008).
5. S.C. Gupta, *The classical Stefan problem*, Elsevier, North-Holland Series, Appl. Math. Mech., Vol. **45** (Elsevier, 2003).
6. G. Caginalp, P. Fife, Phys. Rev. B **33**, 7792 (1986).
7. C. Domb, M.S. Green, *Phase Transitions and Critical Phenomena*, Vol. **5** (Academic Press, London, 1976).
8. M. Fisher, Rev. Mod. Phys. **46**, 597 (1974).
9. D. Jasnow, Rep. Prog. Phys. **47**, 1061 (1984).
10. Steinhardt *et al.*, Phys. Rev. B **28**, 784 (1983).
11. Frenkel *et al.*, J. Chem. Phys. **104**, 9932 (1996).
12. Bolhuis *et al.*, Phys. Rev. Lett. **94**, 235703 (2005).
13. Meloni *et al.*, Phys. Rev. B **83**, 235303 (2011).
14. J. Swift, P.C. Hohenberg, Phys. Rev. A **15**, 851 (1993).
15. K.R. Elder, M. Katakowski, M. Haataja, M. Grant, Phys. Rev. Lett. **88**, 245701 (2002).
16. K.R. Elder, M. Grant, Phys. Rev. E **70**, 051605 (2004).
17. K.R. Elder, N. Provatas, J. Berry, P. Stefanovic, M. Grant, Phys. Rev. B. **75**, 064107 (2007).
18. P.M. Stefanovic, M. Haataja, N. Provatas, Phys. Rev. Lett. **96**, 225504 (2006).
19. J. Berry, M. Grant, K.R. Elder, Phys. Rev. E **73**, 031609 (2006).
20. K. Elder, Lecture Notes, Summer School of DFG Priority Program 1296 *Heterogenous Nucleation*, Herzogenrath, Germany, July 28th to August 1st (2008).
21. S. van Teeffelen, R. Backofen, A. Voigt, H. Löwen, Phys. Rev. E **79**, 051404 (2009).
22. S.A. Brazovskii, Zh. Eksp. Teor. Fiz. **68**, 175 (1975).
23. R. Prieler, J. Hubert, D. Li, B. Verleye, R. Haberkern, H. Emmerich, J. Phys.: Condens. Matter **21**, 464110 (2009).
24. M.A. Choudhary, D. Li, H. Emmerich, H. Löwen, J. Phys.: Condens. Matter **23**, 265005 (2011).
25. R. Evans, Adv. Phys. **28**, 143 (1979).
26. H. Löwen, Phys. Rep. **237**, 249 (1994).
27. H. Löwen, J. Phys.: Condens. Matter **14**, 11897 (2002).
28. Y. Singh, Phys. Rep. **207**, 351 (1991).
29. By scaling, hard ellipsoids with fixed orientation are formally equivalent to hard-sphere systems. This is no longer true, of course, if the interactions are soft and involve an explicit energy scale.
30. A.M. Bohle, R. Holyst, T. Vilgis, Phys. Rev. Lett. **76**, 1396 (1996).
31. H. Löwen, Phys. Rev. Lett. **72**, 424 (1994).
32. H. Löwen, J. Chem. Phys. **100**, 6738 (1994).
33. T. Kirchhoff, H. Löwen, R. Klein, Phys. Rev. E **53**, 5011 (1996).
34. S. Prestipino, F. Saija, J. Chem. Phys. **126**, 194902 (2007).
35. D. van der Beek, P. Davidson, H.H. Wensink, G.J. Vroege, H.N.W. Lekkerkerker, Phys. Rev. E **77**, 031708 (2008).
36. V.N. Manoharan, M.T. Elsesser, D.J. Pine, Science **301**, 483 (2003).
37. E. Bianchi, J. Largo, P. Tartaglia, E. Zaccarelli, F. Sciortino, Phys. Rev. Lett. **97**, 168301 (2006).
38. E. Allahyarov, H. Löwen, A.A. Louis, J.-P. Hansen, Europhys. Lett. **57**, 731 (2002).
39. E. Allahyarov, H. Löwen, J.-P. Hansen, A.A. Louis, Phys. Rev. E **67**, 051404 (2003).
40. M. Rex, H.H. Wensink, H. Löwen, Phys. Rev. E **76**, 021403 (2007).
41. M.M. Tirado, C.L. Martinez, J.G. de la Torre, J. Chem. Phys. **81**, 2047 (1984).

42. H. Löwen, Phys. Rev. E **50**, 1232 (1994).
43. T.V. Ramakrishnan, M. Yussouff, Phys. Rev. B **19**, 2775 (1979).
44. A. Jaatinen, C.V. Achim, K.R. Elder, T. Ala-Nissila, Phys. Rev. E **80**, 031602 (2009).
45. A.D.J. Haymet, D.W. Oxtoby, J. Chem. Phys. **74**, 2559 (1981).
46. B.B. Laird, J.D. McCoy, A.D.J. Haymet, J. Chem. Phys. **87**, 5449 (1987).
47. P. Harrowell, D. Oxtoby, J. Chem. Phys. **80**, 1639 (1984).
48. Y.C. Shen, D. Oxtoby, J. Chem. Phys. **105**, 6517 (1996).
49. Y.C. Shen, D. Oxtoby, J. Chem. Phys. **104**, 4233 (1996).
50. K.-A. Wu, A. Adland, A. Karma, Phys. Rev. E **81**, 061601 (2010).
51. G.I. Tóth, G. Tegze, T. Pusztai, G. Tóth, L. Gránásy, J. Phys.: Condens. Matter **22**, 364101 (2010).
52. A. Jaatinen, T. Ala-Nissila, J. Phys.: Condens. Matter **22**, 205402 (2010).
53. M. Greenwood, J. Rottler, N. Provatas, Phys. Rev. E. **83**, 031601 (2011).
54. M. Plapp, Philos. Mag. **91**, 25 (2011).
55. M. Haataja, L. Gránásy, H. Löwen, J. Phys.: Condens. Matter **22**, 360301 (2010).
56. U.M.B. Marconi, P. Tarazona, J. Chem. Phys. **110**, 8032 (1999).
57. H. Löwen, J. Phys.: Condens. Matter **15**, V1 (2003).
58. G.H. Fredrickson, K. Binder, J. Chem. Phys. **91**, 7265 (1989).
59. N.A. Gross, M. Ignatiev, B. Chakraborty, Phys. Rev. E **62**, 6116 (2000).
60. R. Backofen, A. Voigt, J. Phys.: Condens. Matter **22**, 364104 (2010).
61. J. Hubert, M. Cheng, H. Emmerich, J. Phys.: Condens. Matter **21**, 464108 (2009).
62. J.F. Lutsko, G. Nicolis, Phys. Rev. Lett. **96**, 046102 (2006).
63. H.J. Schöpe, G. Bryant, W. van Megen, Phys. Rev. Lett. **96**, 175701 (2006).
64. T.H. Zhang, X.Y. Liu, J. Am. Chem. Soc. **129**, 13520 (2007).
65. T. Schilling, H.J. Schöpe, M. Oettel, Phys. Rev. Lett. **105**, 025701 (2010).
66. L. Gránásy, G. Tegze, G.I. Tóth, T. Pusztai, Philos. Mag. **91**, 123 (2011).
67. P. Dillmann, G. Maret, P. Keim, J. Phys.: Condens. Matter **20**, 404216 (2008).
68. M.I. Mendelev, J. Schmalian, C.Y. Wang, J.R. Morris, K.M. Ho, Phys. Rev. B **74**, 104206 (2006).
69. M. Dzugutov, Phys. Rev. A **46**, 2984 (1992).
70. C.V. Achim, M. Karttunen, K.R. Elder, E. Granato, T. Ala-Nissila, S.C. Ying, Phys. Rev. E. **74**, 021104 (2006).
71. J.A.P. Ramos, E. Granato, C.V. Achim, S.C. Ying, K.R. Elder, T. Ala-Nissila, Phys. Rev. E **78**, 031109 (2008).
72. G. Tegze, L. Gránásy, G.I. Tóth, J.F. Douglas, T. Pusztai, Soft Matter **7**, 1789 (2011).
73. G. Tegze, G.I. Tóth, L. Gránásy, Phys. Rev. Lett. **106**, 195502 (2011).
74. W.B. Rusell, P.M. Chaikin, J. Zhu, W.V. Meyer, R. Rogers, Langmuir **13**, 3871 (1997).
75. G. Tegze, G. Bansel, G.I. Tóth, T. Pusztai, Z. Fan, L. Gránásy, J. Comput. Phys. **228**, 1612 (2009).
76. T. Pusztai, G. Tegze, G.I. Tóth, L. Környei, G. Bansel, Y. Fan, L. Gránásy, J. Phys.: Condens. Matter **20**, 404205 (2008).
77. S. Muralidharan, M. Haataja, Phys., Rev. Lett. **105**, 126101 (2010).
78. T. Hirouchi, T. Takaki, Y. Tomita, Comp. Mat. Sci. **44**, 1192 (2009).
79. P.F. Tupper, M. Grant, EPL **81**, 40007 (2008).
80. S.K. Mkhonta, D. Vernon, K.R. Elder, M. Grant, arXiv:0806.3445v2.
81. R. Wittkowski, H. Löwen, H.R. Brand, Phys. Rev. E **82**, 031708 (2010).
82. H. Löwen, J. Phys.: Condens. Matter **22**, 364105 (2010).
83. H. Assadi, unpublished.